A Novel 3-D Indoor Ray-Tracing Propagation Model: The Path Generator and Evaluation of Narrow-Band and Wide-Band Predictions

Georgia E. Athanasiadou, *Member, IEEE,* and Andrew R. Nix, *Associate Member, IEEE*

***Abstract*—A novel three-dimensional (3-D) ray-tracing model capable of supporting detailed representation of the indoor environment, as well as external building structures, is presented in this paper. The developed algorithm uses a hybrid imaging technique where the two-dimensional (2-D) image generations in vertical and horizontal planes are combined to produce 3-D paths. It also employs the concept of "illumination zones" of the images which greatly simplifies the image map and allows the evaluation of complex indoor scenarios.**

In order to investigate the accuracy of the presented model, comparisons of predictions with narrow-band and wide-band measurements are performed in line-of-sight (LOS), non-LOS (NLOS), and deep shadow areas, both for co- and cross-polarized antennas. The analysis shows that accurate power predictions can be achieved for both antenna polarizations with rms errors less than 7 dB, even when long sections of the test route are in deep shadow areas. There is a trend agreement between the simulated and measured channel impulse responses, while the rms delay spread in NLOS areas is predicted with less than 5-ns rms error (or better than 13% normalized mean error). The paper provides an insight into the real and the modeled radio channel.

***Index Terms*—Narrow-band and wide-band indoor radio channel measurements and predictions, propagation modeling, ray tracing.**

I. Introduction

In THE forthcoming years, the market for indoor wireless networking facilities is expected to grow considerably in both commercial and domestic sectors. At present, there is a great deal of research focused on the development of future wireless access systems, particularly on the design of wireless LAN's which support data rates in excess of 100 Mbps. It is exactly because of the requirement for wide-band as well as narrow-band characterization of the radio channel for the development and planning of these systems, and also due to the site specific nature of the indoor operational environments, that ray-tracing methods have emerged as the dominant techniques to predict propagation in such environments. Ray tracing produces deterministic channel models that operate by processing user-defined environments. In recent years, many authors have investigated the application of ray tracing to predict the amplitudes, time delays, and arrival angles of the various multipath components for indoor and outdoor scenarios [1]–[11].

This paper presents a novel three-dimensional (3-D) ray-tracing propagation algorithm for single floor scenarios that allows the rapid generation of complex channel impulse response characteristics. In Section II, the basic theory for this propagation model and the associated path generator are presented. It is shown how 3-D rays are produced by combining the results of two two-dimensional (2-D) ray-tracers, one in the horizontal and one in the vertical plane. This section also explains how the algorithm is greatly enhanced by associating each image with a specific area, known as the image's "illumination zone." The accuracy of the presented model is then investigated with comparisons of predictions with measurements performed in line-of-sight (LOS), non-LOS (NLOS), and deep shadow areas, both for co- and cross-polarized antennas. Section III describes the site of the field trials and explains the need for relatively detailed representation of the indoor environments. In Section IV, power results are compared with narrow-band measurements taken inside and outside the building. It is illustrated that there are some problematic areas for the ray-tracing algorithms, arising due to the modeling of the walls as infinitely thin. Finally, Section V presents comparisons of simulated and measured channel impulse responses and rms delay spread values and describes differences between the channel characteristics for co- and cross-polarized antennas.

II. The Ray-Tracing Algorithm

A. Basic Theory for the Propagation Model

Ray tracing is a technique based on *geometrical optics* (GO's), an easily applied approximate method for estimating a high-frequency electromagnetic field [12]. GO assumes an infinite frequency for the propagating signal, and hence, the dissipating energy can be considered to be radiating in infinitesimally small tubes, often called *rays*. In GO, only direct, reflected, and refracted rays are considered, and, consequently, abrupt transition areas occur, corresponding to the boundaries of the regions where these rays exist. The *geometrical theory of diffraction* (GTD) [13] and its uniform extension, the *uniform GTD* (UTD) [14], [15] complement the GO theory by introducing a new type of ray, known as the diffracted ray. The purpose of these rays is to remove the field discontinuities and to introduce proper field corrections, especially in the zero field areas predicted by GO.

Manuscript received May 3, 1999; revised September 13, 1999. The work of G. E. Athanasiadou was performed during her Ph.D. studies at the University of Bristol and supported in part by NORTEL, Harlow, U.K.

G. E. Athanasiadou is with Adaptive Broadband Ltd., Cambridge, CB4 1YG, U.K. (e-mail: gathanasiadou@adaptivebroadband.com; gathanasiadou@hotmail.com).

A. R. Nix is with the Centre for Communications Research, University of Bristol, Bristol BS8 1UB, U.K.

Publisher Item Identifier S 0018-9545(00)03680-X.

In a wireless communications system, the signal arriving at the receiving antenna consists of several multipath components, each of which is the result of the interaction of the transmitted waves with the surrounding environment. The application of GO and UTD to a given propagation problem requires that the given configuration is decomposed into simple geometrical configurations for which the reflection, transmission, and diffraction coefficients can be calculated. All rays contributing significantly to the channel characterization must be traced, and the complex impulse response $h(t)$ of the radio channel is then found as the sum of these contributions [16]

$$h(t) = \sum_{n=1}^{N} A_n \delta(t - \tau_n) \exp(-j\vartheta_n). \tag{1}$$

Here, the received signal $h(t)$ is formed by N time-delayed impulses (rays), each represented by an attenuated and phase-shifted version of the original transmitted impulse. For each ray, the model computes the amplitude A_n, the arrival time τ_n, and phase ϑ_n. According to the objects encountered by the ith ray, its complex received field amplitude E_i (V/m) is given by

$$E_i = E_0 F_{ti} F_{ri} \{\Pi_j R_j \Pi_k T_k \Pi_l A_l(s', s) D_l\} \frac{e^{-jkd}}{d} \tag{2}$$

where E_0 represents the reference field, F_{ti} and F_{ri} the transmitting and receiving antenna field radiation patterns in the direction of the ray, R_j the reflection coefficient for the jth reflector, T_k the wall transmission coefficient for the kth transmission, D_l the diffraction coefficient for the lth diffracting wedge, and e^{-jkd} the propagation phase factor due to the path length $d, (k = 2\pi/\lambda$, with λ representing the wavelength) [12]. The diffraction coefficients are also multiplied by a factor $A_l(s', s)$, which gives the correct spatial attenuation of the diffracted rays, given the $1/d$ dependence in the last term (s' and s are the path lengths before and after the diffraction point) [15]. For the calculation of the coefficients, each wall is characterized by its permittivity, conductivity and thickness. Moreover, all coefficients in (2) are found as functions of the angles of incidence (Fig. 1).

An advantage of ray-tracing algorithms over other propagation models is the ability to incorporate antenna radiation patterns and particularly, as shown in (2), to consider the effect of the radiation pattern on each ray individually. Since in this algorithm the geometry of each ray is examined in 3-D space, both the azimuth and elevation angles of arrival at the antennas are available, and, hence, 3-D radiation patterns can be used. Moreover, in this model the antennas can be steered in any direction in space and hence, the channel can be examined for any antenna orientation. Note that the algorithm works with the electromagnetic field of the rays and hence, uses the complex radiation patterns of the field components. This feature, in conjunction with the fact that all reflections, transmissions, and diffractions are computed using 3-D vector mathematics, makes the model very useful in the study of different antenna polarizations and the examination of depolarization effects.

B. The Path Generator

As previously explained, ray tracing represents electromagnetic waves as rays which are generated and launched in 3-D space from the transmitting antenna. In order to trace the ray paths, in this model a technique based on the electromagnetic theory of images [3], [4] has been developed. Rather than using the *ray launching* approach [5], [8], where rays are sent out at various angles and their paths are traced until a certain power threshold is reached, the technique adopted here considers all walls and obstacles as potential reflectors and evaluates the location of their base-station images. This imaging technique works by generating an image table for each base-station

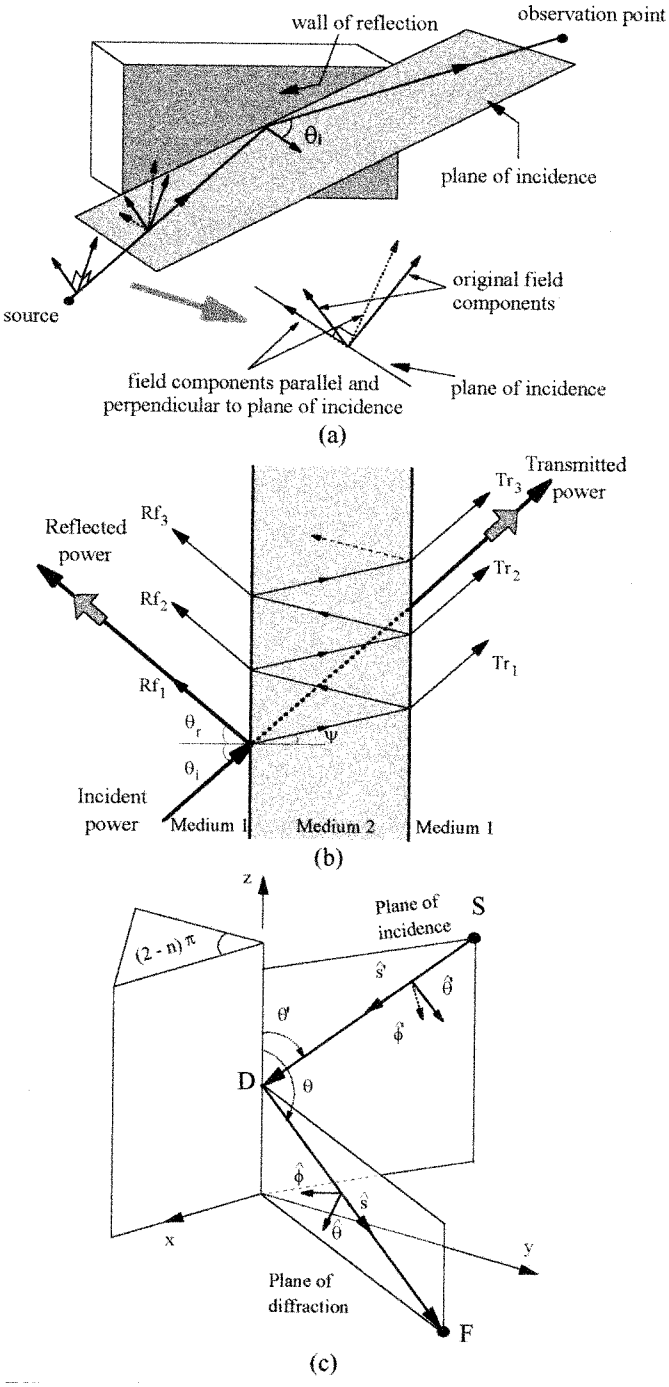

Fig. 1. Modeling the ray interactions with the simulated environment. (a) *Plane of incidence* of a uniform wave incident at an oblique angle on an interface. (b) Transmitted and reflected rays for an oblique incident wave on a conducting dielectric slab. (c) Ray-fixed coordinate systems in the case of diffracted rays.

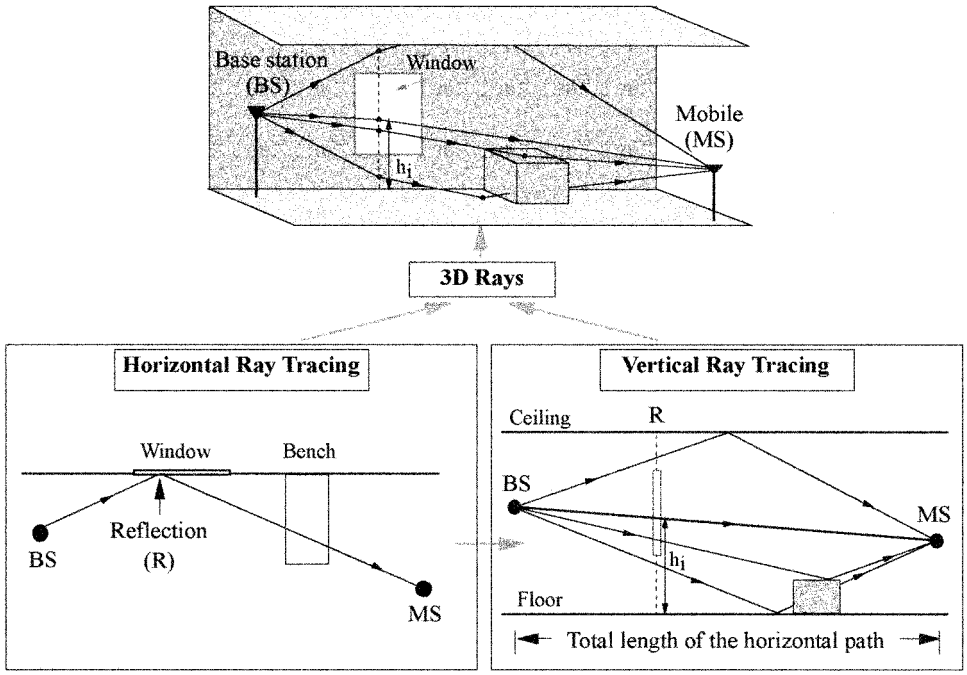

Fig. 2. A 2-D/3-D hybrid analysis.

location, considering all the various wall reflection, transmission, and diffraction permutations that are possible in a given area. The image information is then stored and used to compute the channel characteristics at each mobile location. The use of such an image map dramatically improves the operating speed of the algorithm since repetitive calculations no longer have to be performed.

In this model, a hybrid imaging technique has been developed according to which 2-D image generations in vertical and horizontal planes are combined to produce 3-D paths, as shown in Fig. 2. First, horizontal ray tracing finds all possible paths in 2-D space. All vertical walls are included in this analysis and considered as infinitely tall, even if they do not extend from floor to ceiling (i.e., partitions, side surfaces of benches, etc.). To allow 3-D paths to be found, vertical ray tracing is performed based on the results of the horizontal analysis. For every path found in the horizontal plane, ray tracing in the vertical plane takes place where the position of the reflections off the horizontal surfaces are calculated, and the height of each reflection, transmission, or diffraction point both for the direct and the rays with vertical reflections is determined. Hence, a path found by the horizontal ray tracing, corresponds to many 3-D rays with multiple vertical reflections. For example, in Fig. 2, the ray found by the horizontal ray tracing, corresponds to four rays in 3-D, if up to one reflection is allowed in the vertical plane. The vertical analysis also determines how the results of the horizontal ray tracing apply on each of these rays. For instance, if the horizontal analysis indicates a transmission and a reflection, the vertical ray tracing determines for each of the resulting 3-D rays, whether the ray transmits through or passes above a wall, or whether a ray is not valid because the reflection takes place outside the vertical limits of the reflection wall. Hence, only one of the 3-D rays in Fig. 2 passes through the work bench as suggested by the horizontal analysis, and also two of these rays reflect on the window and the rest on the wall at a height which is indicated by the vertical analysis. The vertical ray tracing also works with image theory but without the diffraction effects. The maximum number of allowable transmissions, reflections, diffractions, and also reflections in the vertical plane for each path is defined by the user.

With this hybrid analysis, the algorithm is able to support the modeling of the ceiling, floor, and other horizontal surfaces, such as tables and benches. It also supports walls with multiple windows and doors and also partitions (i.e., walls with heights less than the ceiling). The model allows the width, height, and position of each object to be defined. Furthermore, rays whose paths fall partially outside of the buildings are modeled and external building structures can also be considered [6]. The model has been optimized for use in single floor indoor scenarios. The algorithm can be extended to support multiple floors, but if each floor has a completely different structure then the complexity of the model will be prohibitive. To ensure as generic a model as possible, wall transmission and corner diffraction are fully supported even for onward propagating cases, i.e., each wall transmission or corner diffraction can undergo subsequent diffractions, reflections, and transmissions. Although for outdoor studies wall transmission is often ignored, for indoor analyses transmission is an important propagation mechanism, particularly for NLOS locations.

One of the most significant characteristics of the model presented here is that each image is associated with a specific *illumination zone*, i.e., the area for which the image can give a valid path (Fig. 3). This new information reduces the number of images and the time for path tracing significantly and makes it feasible for the model to study large complicated environments and trace thousands of rays within seconds. Similar methods are used by the models presented in [9], [11], and [17] in order to produce efficient algorithms. With this technique, only walls

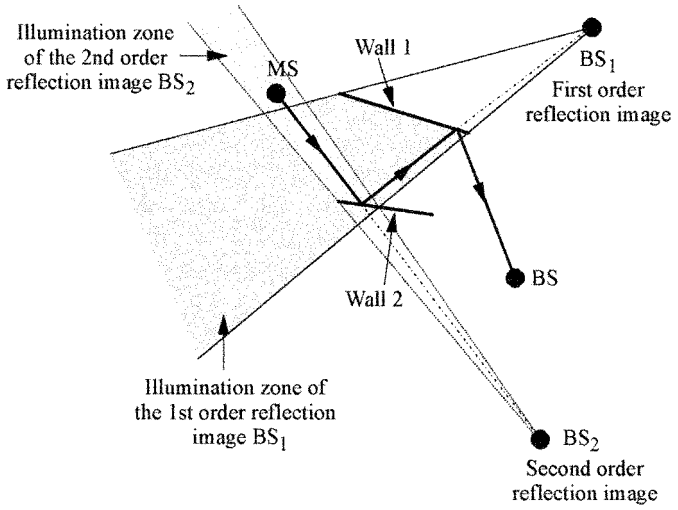

Fig. 3. Image generation and the illumination zones of the images. The basic concept and the path tracing using illumination zones.

and corners inside the illumination zone of the image can be used for the formation of new images, and moreover, these new images are not valid for the entire wall, but only for the part of the wall illuminated by the *parent* image. The illumination zones of high-order reflection images tend to become narrower and this prevents the number of images from increasing exponentially with the order of ray interactions with the environment. Hence, the number of images is reduced dramatically since only images which are capable of producing valid paths are generated and stored in the image table.

Using illumination zones, the time for path tracing is reduced not only because the model has to search for valid paths among fewer images, but also because the images which illuminate a mobile position can now be found very easily with a simple test. In order to find out whether an image can give a viable ray, instead of having to trace each possible ray all the way back to the base station, find the points of intersection with the corresponding walls and examine whether they are valid, the algorithm has only to check whether the mobile lies inside the illumination zone of the image. Once the above check with the last image of the path is completed, it is established whether a valid path can be produced and no further examinations for the rest of the images along the path are necessary. As a result, the model does not waste time tracing paths with many orders of reflection, only to find out at the last image that these paths cannot exist. For example, in Fig. 3, for the examined mobile position (MS), the image BS_2 can give a valid path, while BS_1 cannot, because the mobile is inside the illumination zone of BS_2 and outside the zone of BS_1. When the mobile is in the illumination zones of both the images of the horizontal and vertical analysis, a ray path exists and the model starts calculating its electromagnetic field.

The model runs on UNIX machines (SUN Ultra 1) and although it is a research code that has not been optimized for speed, it takes less than a second for a point prediction even with many orders of reflections, diffractions, and transmissions. However, when horizontal surfaces are added to the model (other than the floor and the ceiling), the speed is reduced. The reason is that although the image tree for the horizontal and the vertical ray tracing is generated once for a specific base-station position and then is stored and used for all the predictions, when a ray path passes through areas with horizontal surfaces, the algorithm has to generate online a new image tree for the vertical ray tracing.

III. The Measurement Site and the Representation of the Area in the Model

In order to evaluate the performance of the model, simulation results are compared in this section with narrow-band measurements performed in the M.Sc. lab of the University of Bristol. The lab is on the ground floor of Queen's Building, a 40-yr old building of traditional architecture with thick walls, high windows, differing ceiling heights in each room, and generally many features that are difficult to model. Fig. 4 shows the ground plan of the area as represented in the model. The region around the lab has also been included in the database. The dimensions of the entire simulated area are approximately 125×80 m. The representation of the environment in the model is more detailed around the transmitter and the sites where the measurements took place. In order to fully visualize the environment, Fig. 5 depicts a 3-D view of the lab as modeled in the simulation. For this study, not only are the windows and doors included in the database, but also the benches and all major metallic objects.

At low frequencies and for narrow-band systems, a simple representation of an indoor environment could be sufficient. However, indoor propagation tools must evolve in order to meet the challenging requirements of next generation wireless systems. Future indoor communication systems will be wideband, operating at 5 and 17 GHz (i.e., IEEE 802.11 and HIPERLAN) [18], [19] and possibly as high as 60 GHz [20]. At such high frequencies, the dimensions of large objects become comparable with the wavelength of the signal, and, hence, a more detailed representation of the environment is necessary. Generally, ray-tracing models assume empty rooms and do not include the effects of furniture, mainly because the furniture locations and characteristics are often unknown or unavailable, and if considered, the complexity of the simulation increases immensely. However, the effect of large objects on the radio channel may be very significant and also the signal characteristics will be different in an open area than in an area filled with furniture [20]. According to the radar cross section theory, the power reflected from an object depends on its shape, size, and orientation with respect to the incident signal as well as its material properties [21]. Hence, the criteria for the inclusion of an object in the database of the model should not only consider the size, but also the material and position. For instance, objects such as metallic cabinets are strong reflectors, and as such they cannot be ignored when they are in close proximity to the antennas. However, since it is not feasible to consider all objects in the database, this detail is confined to the main area of interest, while the clutter loss associated with other rooms is incorporated to the simulated materials for their walls.

In the lab, the benches and the cabinets are 0.9 and 1.33 m high, respectively. Although the various rooms in the building

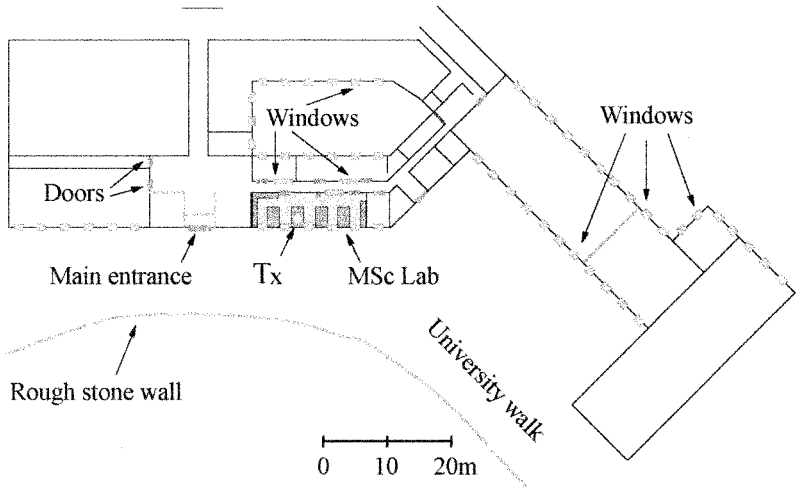

Fig. 4. Ground plan of the environment under investigation.

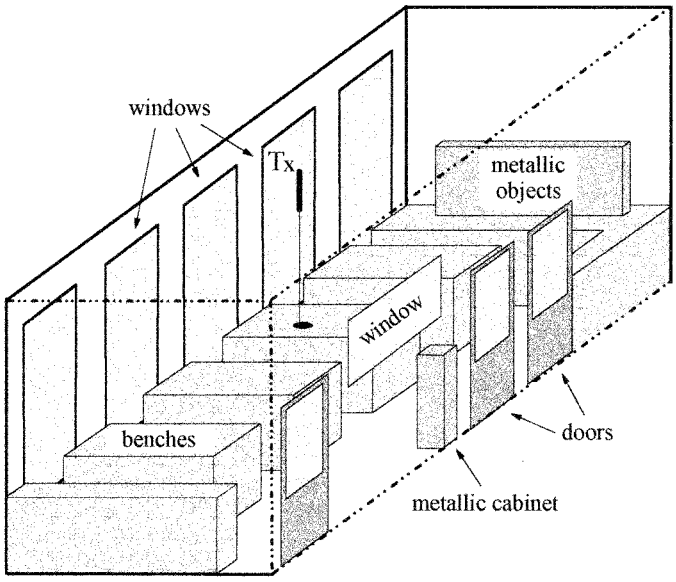

Fig. 5. Three-dimensional representation of the environment.

TABLE I
THE MATERIAL CHARACTERISTICS USED IN THIS STUDY

	Conductivity (S/m)	Relative permitivity	Thickness (cm)
Ceiling	0.005	3	30
Floor	0.00022	7	30
Internal walls	0.005	3	55
External walls	0.005	3	65
Wooden doors	0.0006	2	5
Windows	10^{-10}	6	0.01
Benches	0.015	2	3
Metallic objects	100	3	1
Marble cover	0.00022	7	3
Stone wall	0.005	2.5	30

have different ceiling heights, for the simulation the ceiling is set at a height of 4.6 m for all rooms, which is the height of the ceiling in the lab. The doors are 2.5 m high; they are wooden for the first 1 m and then glass. The external windows are 1.2 m above the floor, their dimensions are 2.4 m by 3.1 m and the distance between them is 1.3 m. As shown in Figs. 4 and 5, there are also internal double-glazed windows between the rooms and the corridor. These are 1.7 m above the floor, and their dimensions are approximately 3.2 m $\times$ 1 m. At the main entrance, the walls shown in Fig. 4 with light grey color, are wooden for the first 1 m and the rest is glass. Unlike the rest of the internal walls, the main entrance walls are covered with marble. Finally, the first 2 m (starting from the main entrance hall) of the corridor passing in front of the lab are covered with wood. These features have all been included in the model because they affect the predictions in the areas of the field trials.

The material characteristics used in this study are shown in Table I. The floor, ceiling, and the various internal and external wall characteristics, are based on different types of stone and brick. The electrical properties and characteristics of the doors, windows and benches are based on wood, glass, and chipboard, respectively [22]–[24]. Since it was the first time that this kind of indoor environment was studied, some measurements were performed initially in order to calibrate the propagation model and determine how to simulate particular features of this environment. Since there are large marble stairs in the simulated area (see Fig. 6), an extra transmission loss of 10 dB was added to their adjacent wall in order to compensate for the attenuation of the rays. Also, except for the lab, all other rooms were modeled empty of furniture. Based on measurements, an extra transmission loss of 3 dB was applied to the walls of the empty rooms, to compensate for this database simplification. Alternatively, different modeled material characteristics could have been chosen for these walls, representing the *effective building*

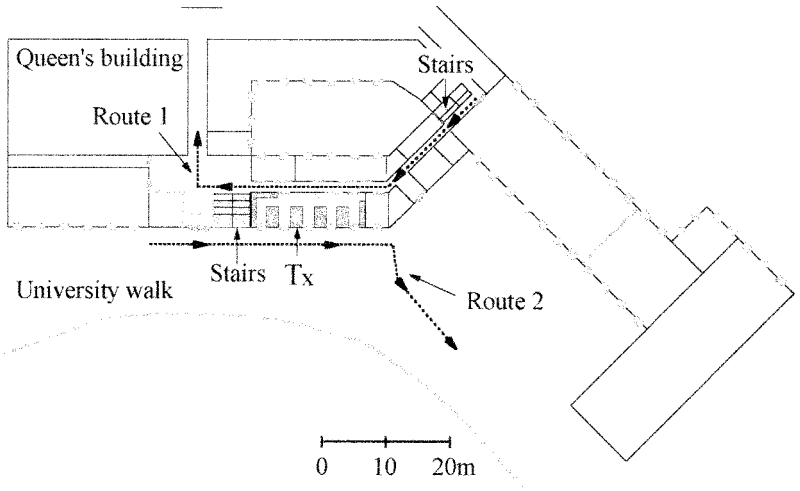

Fig. 6. The routes of the narrow-band measurements.

material properties [5], rather than the actual material of these walls.

IV. Investigation into the Accuracy of the Narrow-Band Predictions

A. Measurement Setup and Methodology

For the measurements, a 30-dBm transmitter (all cable and antenna losses included) was placed at a height of 3 m at location Tx, shown in Fig. 6. The frequency was set at 1.823 GHz and the transmitting antenna was a vertically polarized half-wavelength dipole. The measurements were taken during evenings, in order to avoid much of the temporal variation of the radio channel introduced by people moving around the rooms. Field trials were carried out along two routes, each about 55 m long (Fig. 6). Both routes are in NLOS areas, one inside and the other outside Queen's Building. The first route starts from a deep shadow area away from the transmitter, follows the corridor which passes in front of the lab, enters the main entrance hall, and turns right into another corridor. The second route moves along the pavement outside the building, passing in front of the lab's windows.

The narrow-band receiver was mounted on a trolley which was slowly and carefully driven along the predefined routes. For each route, two sets of measurements were performed: one with a vertical receiving dipole and one with a horizontal dipole always parallel to the route direction. Each set consisted of three consecutive runs along the same route and with the same setup. The values of the received field strength were automatically recorded every 4 cm, and the fast fading was then removed with a sliding window averaging process. In order to preserve the site specific information of the measured data, a five-wavelength window was chosen (equivalent to 83.3 cm). For both receiving polarizations, after the removal of fast fading there was a high degree of correlation between the measured results of the different runs. The correlation coefficient between the measured envelopes of any two runs was between 0.93–0.95 for the vertical and 0.87–0.88 for the horizontal dipole. These numbers illustrate how representative and repeatable these measurements

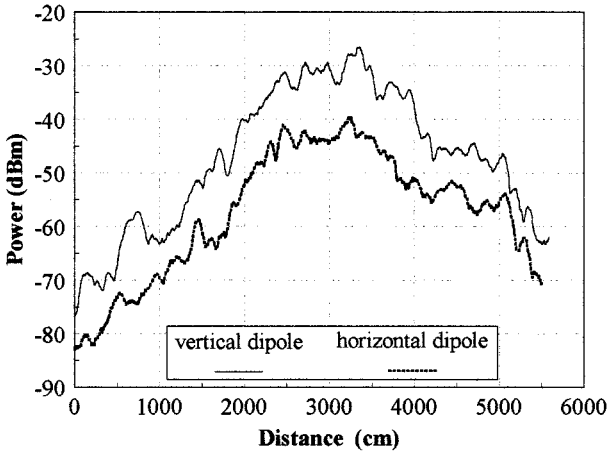

Fig. 7. The average measurements along Route 1 for both receiving antenna orientations.

are for the route under study. By averaging the three runs, the mean measurement is produced which is then used for comparisons with the simulation predictions.

As shown in Fig. 7, the power along Route 1 increases as the receiver moves toward the transmitter, falls and remains fairly constant in the main entrance (~41–51 m), and finally falls even more in the last corridor (~51 m). The steepest changes in power are when the receiver enters or leaves a corridor (~12, 41, and 51 m). The received power for the horizontal dipole is consistently smaller than the power of the vertical dipole. Although the power difference between the differently polarized receivers is around 12 dB for the part of the route closest to the transmitter, it decreases in the distant deep shadowed areas where the relative orientation of the antennas becomes less critical. The power along Route 2 (Fig. 8) peaks when the receiver is in front of the windows close to the transmitter (~15 and 25 m). The measured values for the vertical and horizontal dipoles differ as much as 17 dB. This power difference is larger along Route 2 (outside the building) than along Route 1 (inside the building) because of the lack of the floor–ceiling reflections, which significantly contribute to the received power of the horizontal dipole.

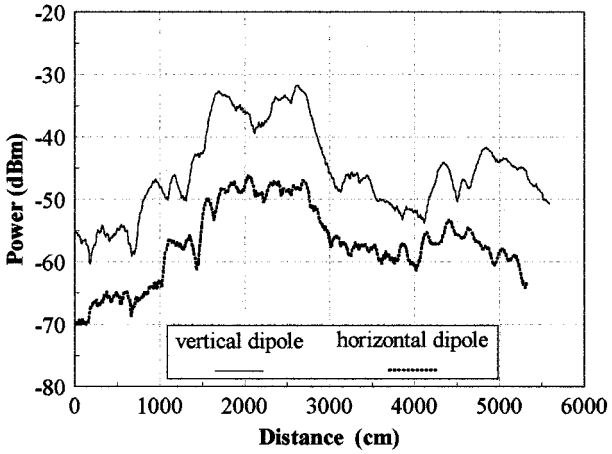

Fig. 8. The average measurements along Route 2 for both receiving antenna orientations.

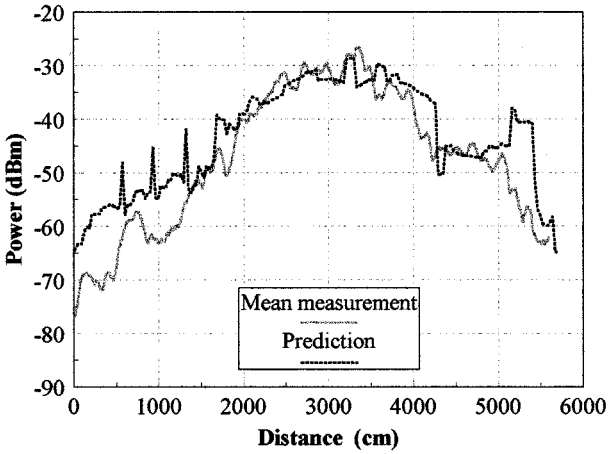

Fig. 9. Measured and predicted power along Route 1 for the copolar case.

B. Model's Setup

All simulation results were obtained for up to four orders of reflection and four orders of wall transmission in the horizontal plane, while each ray could have up to six orders of reflection in the vertical plane. Unlike the field trials, the space resolution between the prediction points was 0.3 m. This is because the predicted power, which is produced as the sum of the power of the rays reaching the receiver, is inherently averaged and no further action is needed to remove the fast fading. Nevertheless, spatial averaging was also used in order to reduce the uncertainty for the receiver position. Hence, as with the measurements, three route studies were performed and their results were averaged to produce the final model predictions. Due to the completely static environment of a ray-tracing model, for each study the route was randomly offset by 30 cm to produce a different set of predictions.

A second set of modeled results was produced by emulating the measurement process. From the predicted complex channel impulse responses every 4 cm, the instantaneous power was produced from the summation of the complex fields of all the rays reaching the receiver. The results obtained in this manner were equivalent to the raw data of a measurement run, and they were processed in the same way. A five-wavelength sliding window was used to remove the fast fading. Three slow fading envelopes were produced which were then averaged to produce a mean predicted envelope similar to the measured one. As with the previous predictions, for each new envelope the route was randomly offset by 30 cm.

C. Measurements and Predictions along Route 1

1) Copolar Antennas: Fig. 9 depicts the mean measured and predicted values along Route 1 for the vertically polarized receiver. It can be seen that the simulation results follow the trend of the measurements throughout the route. As shown in Table II, the mean difference between the predictions and the measurements, calculated with both values in a logarithmic scale, is 4.33 dB with a standard deviation of 5.6 dB. The statistics of the comparison are good given that receiver positions far away from the transmitter in deep shadow areas are also included in the calculations. The poorest agreement between the measurements and the predictions happens toward the beginning of the route, where the model overpredicts the received power by approximately 10 dB. Such a deviation is expected, given that this area is more than 30 m away from the transmitter, with many rooms in between, where the power has to reach the mobile travelling along a lengthy corridor. At the positions in front of the lab (between ∼20 and 40 m), the predicted levels of power are very close to the measurements. Along this part of the route, the mean error is 0.01 dB with a standard deviation of 2.57 dB.

Note that in the areas just before and after the section of the corridor in front of the lab (∼18 and 42 m) and also as the receiver enters the last corridor (∼55 m), the predictions follow the large changes of the measured power levels with a spatial delay. These are *transition regions* which usually exist at the boundaries of the illumination zone of strong rays and happen because of the infinitely thin representation of the walls during the generation of the image tree (this point will become more obvious with the study for Route 2).

The simulation results by emulating the measurement process are depicted in Fig. 10. Even the mean prediction produced by averaging the simulated envelopes varies more than the predictions calculated from the summation of the powers of the rays. Although the difference is small for the majority of the route, it indicates that the averaging of the simulation results emulating the measurement process is still not complete, since it is confined along the route direction. In Fig. 9, the peaks of the predictions from the summation of the ray powers, between 5–15 m, seem to arise due to a single ray which appears at certain points. In ray tracing, the rays are found with geometrical accuracy, and, hence, even rays with only a couple of degrees of visibility will be identified. However, because each value of a slow fading envelope derives from spatial averaging along five wavelengths, the predicted envelopes like the measurements, do not present sudden peaks similar to those appearing at the point predictions.

The error statistics are slightly better for the predicted slow fading envelopes than the results from the summation of the powers. The mean error is 3.57 dB with a standard deviation of 5.84 dB (Table II). Comparing the predictions with the measurements for the 20 m part of the corridor in front of the lab, the mean error is 0.31 dB and the standard deviation is 2.47 dB. The simulation results with the averaged samples keep better track of the mean measurement because they were produced with the

TABLE II
ERROR STATISTICS ALONG ROUTE 1 FOR THE COPOLAR ANTENNAS

	Mean error (dB)	Standard deviation (dB)	RMS error (dB)
Mean prediction along the entire route	4.3388	5.6042	7.0875
Mean prediction along the corridor in front of the lab	0.0123	2.5736	2.5736
Mean predicted envelope along the entire route	3.5710	5.8400	6.8453
Mean predicted envelope along the corridor in front of the lab	0.3164	2.4741	2.4942

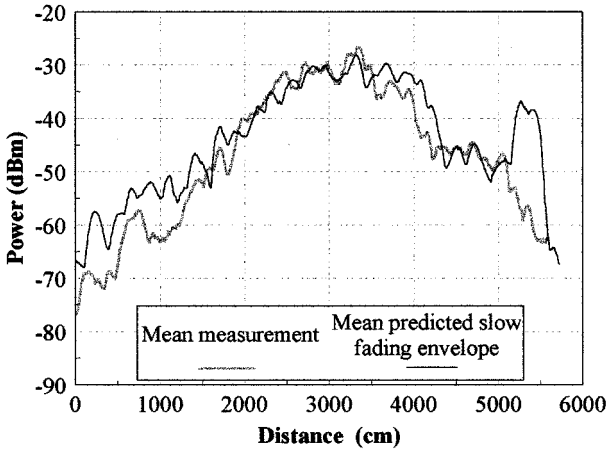

Fig. 10. Mean measured and predicted slow fading envelopes for the copolar case along Route 1.

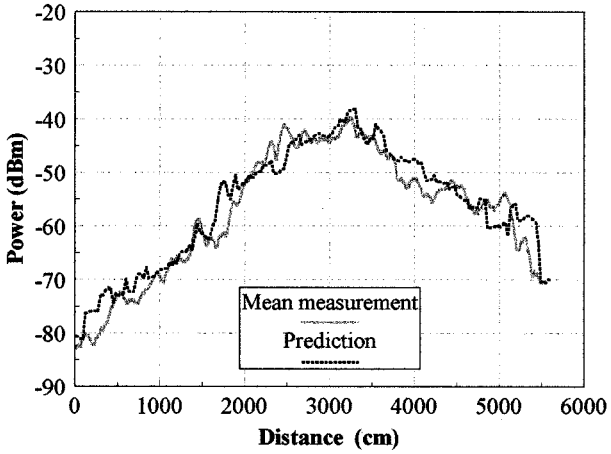

Fig. 11. Measured and predicted power along Route 1 for the cross-polar case.

same sampling and averaging process. Nevertheless, this prediction method was only employed here for comparison purposes and it must be stressed that the power results from the summation of the powers of the rays is the ultimate averaging method [24].

1) Cross-Polar Antennas: Fig. 11 illustrates the measured and predicted power along the same route for a horizontally polarized receiver. The agreement between the measurements and the simulation results is better for the cross-polar than for the copolar case. The predictions are within 3 dB of the measurements for the majority of the route. The mean error is 1.37 dB with a standard deviation of 3.49 dB (Table III). Considering the orientation of the antennas and the position and the length of the test route, the error statistics are very good. By confining the comparison along the 20-m-long corridor in front of the lab, the mean error is 0.22 dB with a standard deviation of 2.54 dB. Fig. 12 depicts the mean prediction produced by averaging the simulated envelopes. As shown in Table III, the errors are similar to those of the predictions from the summation of the ray powers.

Although in total the predictions for the horizontally polarized antenna are better than the predictions for the vertically polarized one, along the corridor in front of the lab the error statistics are better for the copolar case. The transition areas identified earlier for the vertical receiving dipole exist for the horizontal as well, but with less severe impact on the predictions. This is due to the fact that in the case of copolar antennas the power is usually determined by a few dominant rays, while in the cross-polar case, more rays play a critical role. As a result, the changes in power level are not as rapid and abrupt as for the vertical dipole, and the model follows these trends more efficiently.

D. Measurements and Predictions along Route 2—The Illumination Boundaries Problem and the Transition Areas

The measured and predicted power for the co- and cross-polar cases for Route 2 are shown in Figs. 13 and 14, respectively. (The receiver height for this test was 1.17 m.) When both

TABLE III
ERROR STATISTICS ALONG ROUTE 1 FOR THE CROSS-POLAR ANTENNAS

	Mean error (dB)	Standard deviation (dB)	RMS error (dB)
Mean prediction along the entire route	1.3788	3.4919	3.7543
Mean prediction along the corridor in front of the lab	0.2236	2.5495	2.5593
Mean predicted envelope along the entire route	0.6394	3.9510	4.0024
Mean predicted envelope along the corridor in front of the lab	-0.1877	2.7812	2.7875

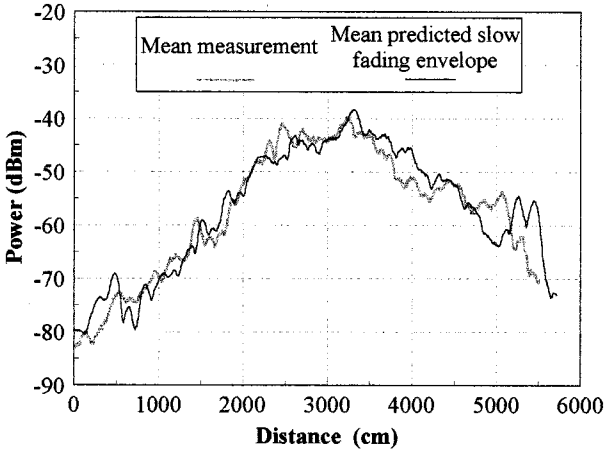

Fig. 12. Mean measured and predicted slow fading envelopes for the cross-polar case along Route 1.

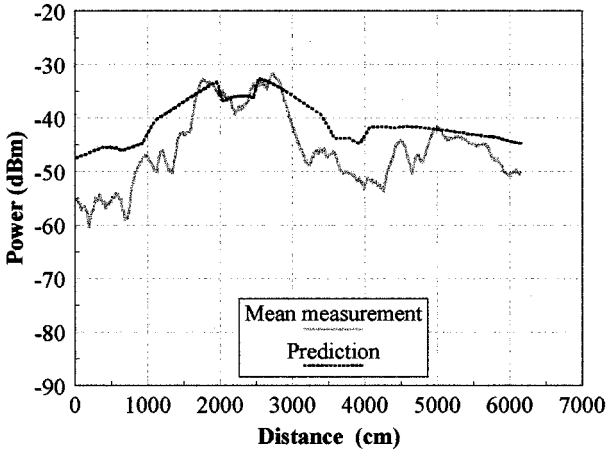

Fig. 13. Mean measurement and prediction along Route 2 for the copolar case.

antennas are vertically polarized, the model overpredicts the power levels for the majority of the route positions. For the cross-polar case, the agreement is better, but there are still some problematic areas, especially at positions close to the external wall of the lab.

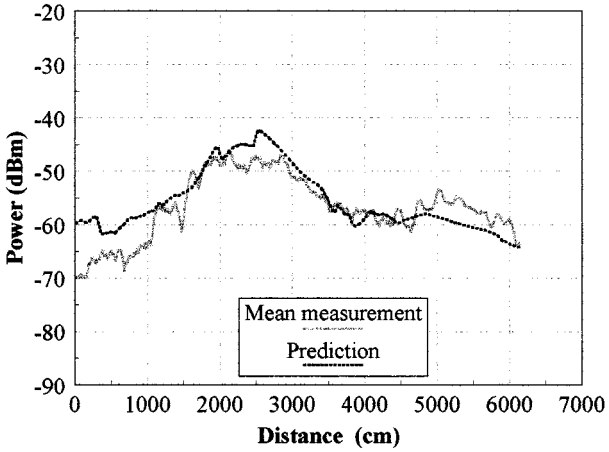

Fig. 14. Mean measurement and prediction along Route 2 for the cross-polar case.

The effects of the assumption of infinitely thin walls in the ray-tracing models become profound in this study. Fig. 15 illustrates the problem by showing the blocking of the illumination of the transmitter caused by the thick walls and how this situation is represented in the model. Assuming that this wall is the external wall of the lab, outside of which the sounder moves along Route 2, then when the receiver is in the ray-tracing illuminated areas, in the model the direct ray between the two antennas is passing through one of the windows with a relatively small loss, compared to the loss of passing through a thick stone wall. However, in the real environment this only happens when the receiver is in the true illuminated areas. The sections of the route inside the ray-tracing illuminated areas are much longer than the sections inside the true illuminated areas. This is the reason why the predicted signal levels are higher than those

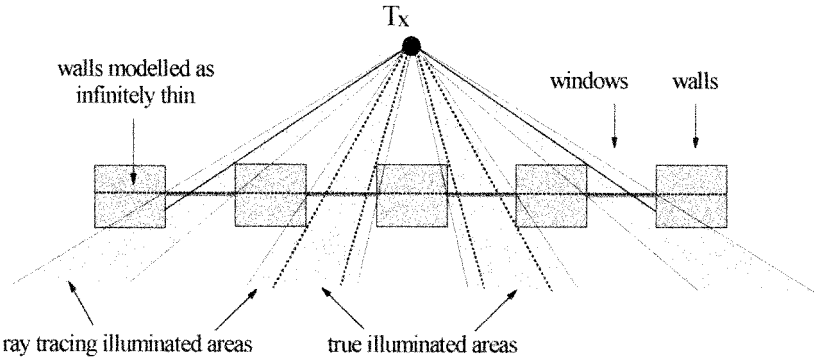

Fig. 15. Problematic areas caused by the assumption of infinitely thin walls.

measured in the majority of the positions in front of the lab in Figs. 13 and 14.

Hence, because of the zero thickness of the simulated walls, not only are the ray-tracing illuminated areas wider than the true illuminated areas, but also exist in places where in reality the illumination zone is totally blocked. The effects of this phenomenon are also obvious along Route 1 inside the building. When there is an illuminated area which, because of the above effect, appears wider in the model, the *transition area* effects arise and the model follows the measurement trend with some spatial delay (e.g., the areas around 18- and 42-m distance in Fig. 9). In the case where an illumination area exists only in the model and not in reality, large peaks and deviations between measurements and predictions occur (like the one just before the receiver enters the last corridor at 52 m from the route start).

The *illumination boundaries problem* is an inherent problem with indoor ray-tracing propagation models. Methods to solve this problem include the modeling of the walls as boxes instead of lines, but the complexity this would introduce is enormous. This phenomenon does not exist for outdoor scenarios where only the outline of the buildings is considered in the model. The problem arises when wall transmission is active and the walls are seen by rays from both sides.

V. Investigation into the Accuracy of the Wide-Band Predictions

A. Comparison Between Measured and Predicted Channel Impulse Responses

In this section, predictions from the indoor model are compared with channel impulse response (CIR) measurements. A network analyzer (HP 8532A) was used for the field trials. Although the measurements were taken in the frequency domain over a bandwidth of 200 MHz, by performing an inverse Fourier transform, the network analyzer results were obtained in the time domain as power versus delay. For this process, the normal window option of the network analyzer was chosen, which gives reduced sidelobes (-44 dB). (Note: the sidelobe reduction is achieved at the expense of increased pulse width.)

The receiving antenna was at a height of 1.8 m, and for each point 16 profiles were measured within an area of 1 m^2. Fig. 17 depicts the 16 measured profiles at the first point together with their mean profile, after being normalized to the peak value. The reason why so many profiles were measured for each point is that

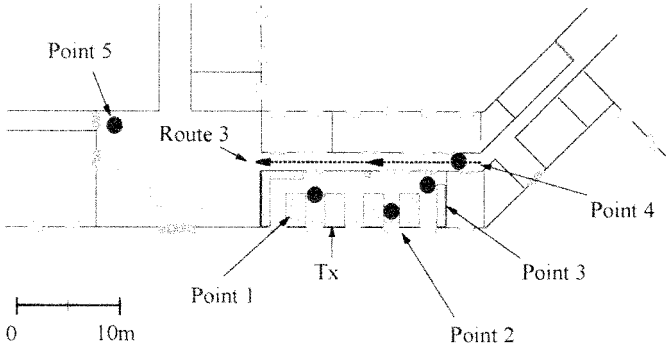

Fig. 16. The points and routes of the wide-band measurements.

the actual profile shape can change significantly over a distance of several centimeters because of the vector addition of the arriving rays with similar delays [11]. The profiles were then processed in order to find a mean measured profile (within a 50-dB power window from the peak value) and its minimum and maximum values at each time sample. With this process the effects of phasor addition and temporal variation are minimized and the site specific comparison becomes feasible. The mean profiles were normalized to their peak value because the main interest for this study was the wide-band behavior of the channel.

The channel impulse responses obtained from the ray-tracing model correspond to measurements made with infinite bandwidth, i.e., each received ray is a perfect impulse in the time domain. To be able to compare simulated results with real measurements, the predicted power profiles were convolved with the impulse response of the network analyzer. In order to calculate the average simulated profile, a grid analysis of 25 points (5×5) was performed over a 1.5 $\times$1.5-m area at each site, similarly with the measurements. This profile was then compared with the mean measured profile. The simmulated results were averaged over a larger area than the measured results in order to reduce the effects of the transition areas. The field trials were performed at five different positions: three in LOS and two in NLOS areas (Fig. 16). With the transmitter always vertically polarized, for each point, two sets of measurements were taken, one with a vertical and one with a horizontal receiving dipole. The direction of the horizontal dipole was always perpendicular to the external wall of the lab. For better understanding of the results in the cross-polar case, Fig. 18 depicts the radiation pattern of a horizontal half-wavelength dipole as calculated in the model for

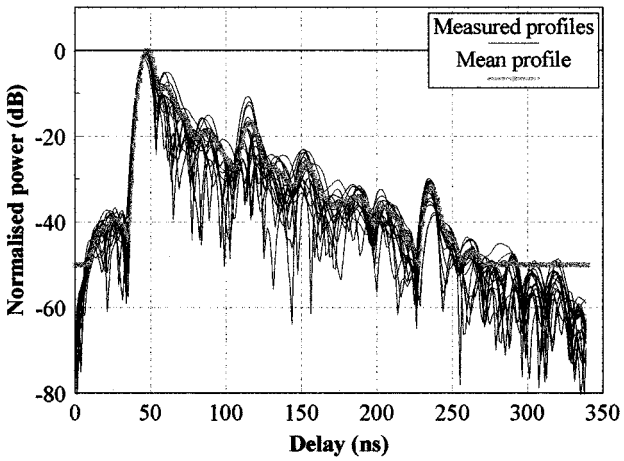

Fig. 17. The 16 measured and mean profiles at Point 1.

the specific antenna orientation. Given that the transmitted field of the vertical dipole has only a vertical component (E_θ), the response of the horizontal receiving dipole is mainly determined by its radiation pattern for E_θ. In this case, the E_ϕ radiation pattern of the receiving dipole only regards multireflected rays which have been depolarized.

1) Results—Point Analysis: The first point, Point 1 in Fig. 16, was by the bench where the transmitter was mounted. Figs. 19 and 20 depict the measured and predicted profiles for the vertical and the horizontal receiving dipole, respectively. It can be seen that the model has predicted all the major power peaks for both polarizations and that the amplitudes of the predicted peaks are very close to the measured ones for the majority of time delays. (Note that it is because of the logarithmic scale of the diagrams, that the mean measurement seems to be closer to the maximum values, while the profile of the minimum measured samples appears to have considerably more variation.) At all points, the profiles for the vertical receiving antenna have large distinct power peaks, while the profiles for the horizontal dipole are relatively flat. This is due to the fact that for the cross-polar case, most rays are of similar powers. The rays with large delays have travelled long distances and the probability of being reflected or transmitted through walls is higher than for the early rays. However, the longer it takes a ray to reach the receiver, the more likely it is for this ray to be blocked in reality. Also, the more a ray interacts with the environment, the more the cumulative error caused by the estimations of the reflection and transmission coefficients increases. As a result, the heavily delayed rays are more difficult to predict. This is not a problem in LOS positions where the channel characteristics are determined by the early dominant rays, but it is certainly an issue under NLOS conditions.

The second measurement was further away from the transmitter, at Point 2 in Fig. 16. The receiver was placed between two work benches, by the lab windows overlooking University Walk. As shown in Fig. 21, for the copolar case, the simulation finds the dominant peaks of the measured profile and follows it for most time delays. Although the second and the third peaks have the right delays, their amplitudes are 8 dB lower than the measured peaks. The most probable reason for this deviation is the assumption of inaccurate material characteristics for a specific part of a wall in the model. The predicted profile for the

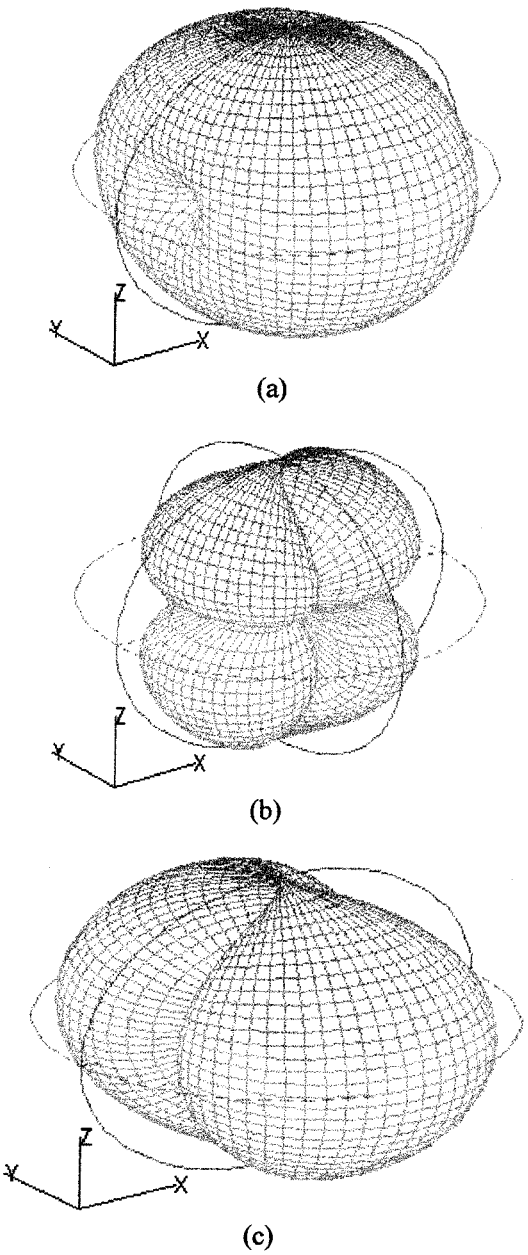

Fig. 18. Three-dimensional radiation patterns (logarithmic scale) of (a) the total power, (b) the power of the vertical (E_θ), and (c) the horizontal (E_ϕ) field components of a horizontal dipole, for the coordinate system of the model.

horizontal dipole, as shown in Fig. 22, is less accurate although still represents a good match. In the cross-polar cases, because the dominant rays are weaker than in the copolar case, the scatterers become more important. On the other hand, in the case of copolar antennas, the power profile is determined by a few dominant rays and if the prediction for one of these rays is inaccurate (because of incorrect coefficient estimation, misplacement of the reflector in the building database, or because during the measurements this ray was blocked by a passing person or a piece of furniture which is not considered in the simulation) then the deviation between measured and predicted profiles will be considerable.

The third point, Point 3 in Fig. 16, illustrates better the remarks mentioned in the above analysis. This point is also in a

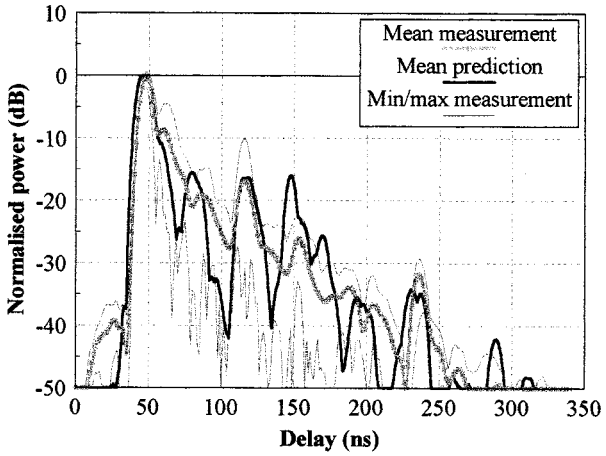

Fig. 19. Measured and predicted CIR's for a vertical receiving dipole at Point 1.

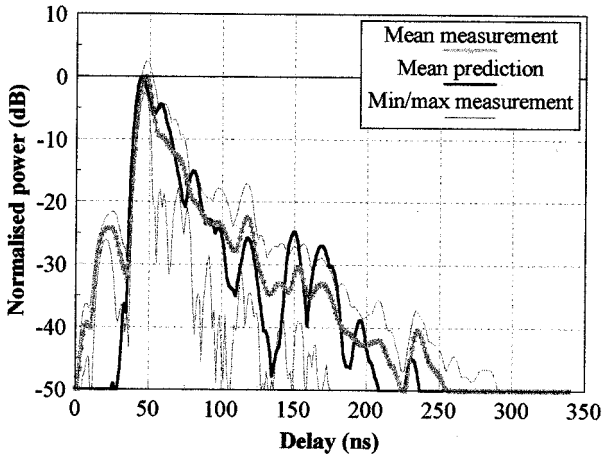

Fig. 20. Measured and predicted CIR's for a horizontal receiving dipole at Point 1.

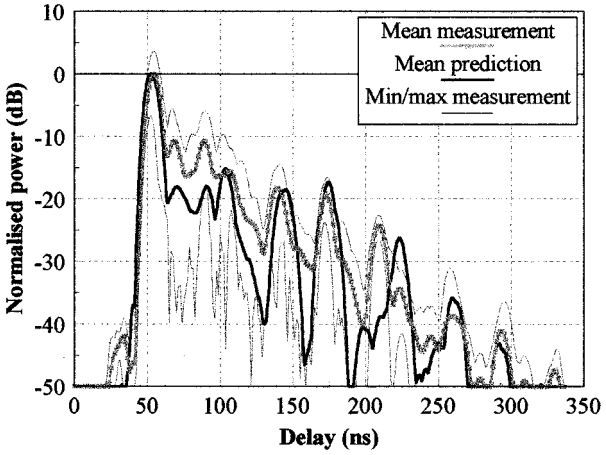

Fig. 21. Measured and predicted CIR's for a vertical receiving dipole at Point 2.

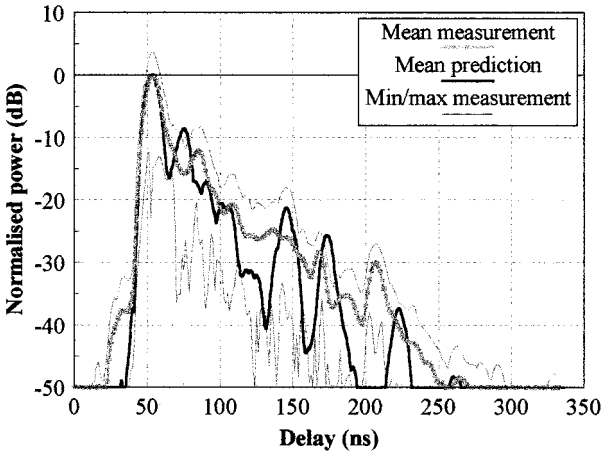

Fig. 22. Measured and predicted CIR's for a horizontal receiving dipole at Point 2.

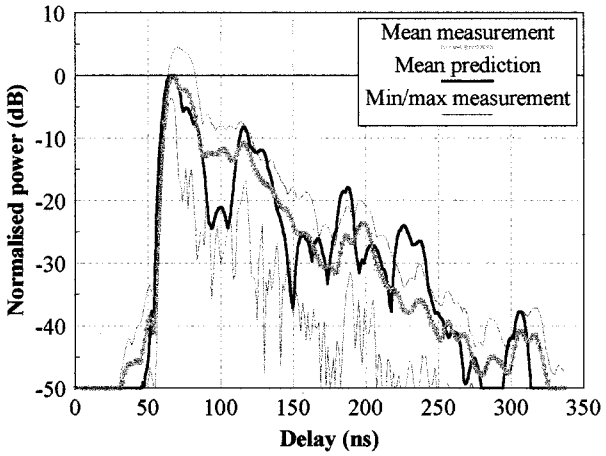

Fig. 23. Measured and predicted CIR's for a vertical receiving dipole at Point 3.

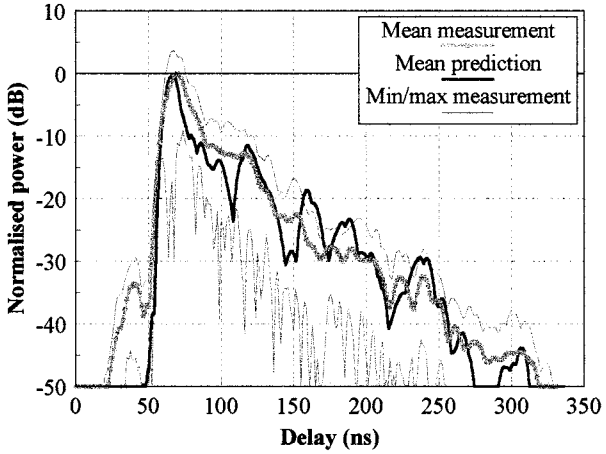

Fig. 24. Measured and predicted CIR's for a horizontal receiving dipole at Point 3.

LOS position and is located at the end of the lab, by the door to the corridor. As shown in Figs. 23 and 24, the simulated profiles remain within the limits of the measured profile for the majority of time delays. The prediction for the horizontal receiver follows closely the mean measured profile, while the prediction for the vertical dipole is not as good. A couple of false predicted dominant rays, at delays around 100 and 230 ns, are enough to change the trend of the predicted profile created by thousands of rays. Unlike the vertical dipole, the predictions for the horizontal dipole are more stable, because they are determined by more rays with similar amplitudes.

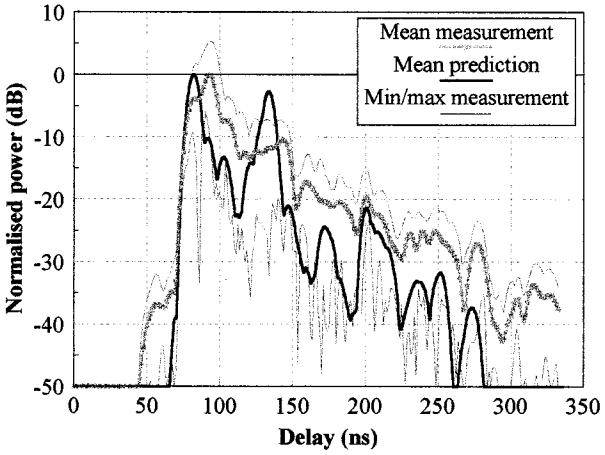

Fig. 25. Measured and predicted CIR's for a vertical receiving dipole at Point 4.

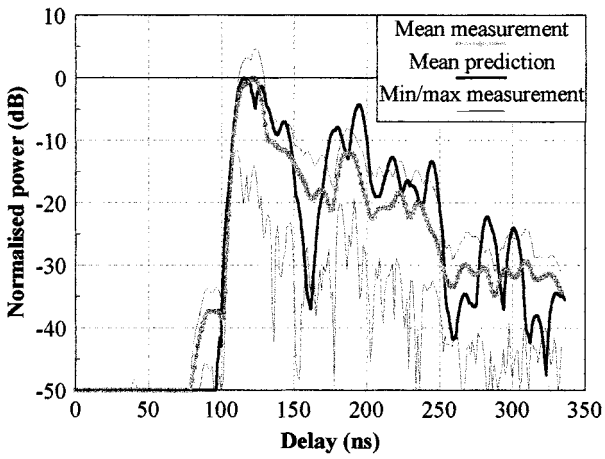

Fig. 27 Measured and predicted CIR's for a vertical receiving dipole at Point 5.

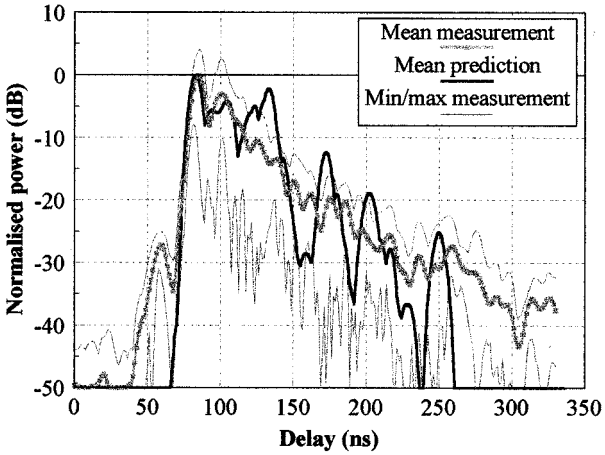

Fig. 26. Measured and predicted CIR's for a horizontal receiving dipole at Point 4.

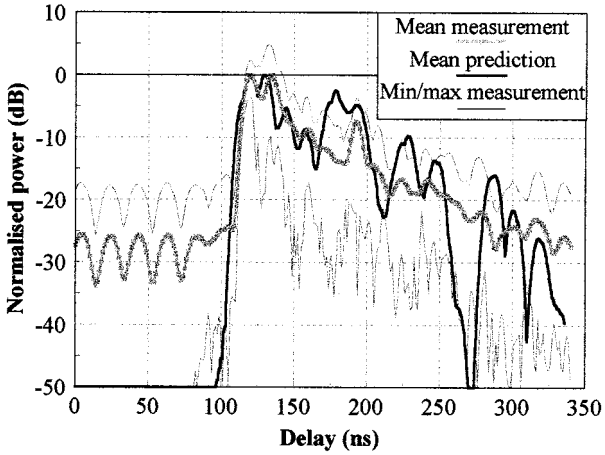

Fig. 28. Measured and predicted CIR's for a horizontal receiving dipole at Point 5.

The first point under NLOS conditions was in the corridor, shown as Point 4 in Fig. 16. Due to its position, rays can reach the area following a number of alternative routes. As Fig. 25 shows, although the simulated power profile follows the same exponential time decay as the measured result, it is about 5 dB lower. This happens because the prediction of the peak value, where the profile has been normalized, is overestimated. The reason why the peak value is overestimated is because Point 4 is in a *transition region* (see Fig. 15). As a result, although in reality there is a thick wall between the transmitter and the receiver, in the simulation it appears to be a thin wooden-glass door. In the case of the horizontal dipole, the simulation results are closer to the measurements, but with large fluctuations around the mean measured profile (Fig. 26). Generally, for the NLOS positions very accurate predictions become more difficult to achieve, not only because of the absence of the direct LOS ray, but also because of the representation of the walls in the model as infinitely thin.

These remarks also hold for the last measured point, Point 5 in Fig. 16, which is a location even farther from the transmitter, at an open area at the entrance of the building. The characteristics of the area around this point have not been modeled in such detail as the lab. Also, the main rays pass through the wall adjacent to the stairs which, as explained earlier, is an area difficult to represent in the model. As it can be seen from the predicted profiles in Figs. 27 and 28, the simulations remain close to the measurements and despite the fluctuations, the predictions tend to follow the trend of the measurements. In the case of the horizontally orientated receiving dipole, the peak of the received signal is only 25 dB above the noise floor, hence increasing the uncertainty of the measurements.

2) Comparison of Measured and Predicted Wide-Band Channel Statistics: The aim is to develop a propagation model able to characterize the radio channel and follow its trends within an acceptable error and standard deviation. In Tables IV and V, the mean value and also the standard deviation and the minimum and maximum rms delay spread of both the measured and the simulated profiles at each individual point are shown. A 30-dB window relative to the peak of the profiles was used for the calculations, except for the case of the measured profiles of the horizontal receiving dipole at the NLOS Point 5, where a 20-dB window was used. (As depicted in Fig. 28, the measured power profile for the cross-polar case at Point 5 is very close to the noise floor, hence, the calculations of the

TABLE IV
STATISTICS OF THE MEASURED AND PREDICTED RMS DELAY SPREAD VALUES (IN NANOSECONDS) OF THE COPOLAR ANTENNAS

Point	Measurements				Predictions			
	mean	std	max	min	mean	std	max	min
1	13.67	2.26	17.98	9.91	14.17	2.83	18.75	7.91
2	22.80	5.19	31.67	14.96	19.59	5.04	32.48	12.08
3	19.24	4.56	26.28	9.75	21.04	5.07	29.16	13.10
4	25.42	4.56	29.49	13.85	23.30	3.64	28.35	16.85
5	25.09	7.68	40.16	13.10	34.18	3.85	40.52	25.75

TABLE V
STATISTICS OF THE MEASURED AND PREDICTED RMS DELAY SPREAD VALUES (IN NANOSECONDS) OF THE CROSS-POLAR ANTENNAS

Point	Measurements				Predictions			
	mean	std	max	min	mean	std	max	min
1	10.77	2.28	14.41	6.76	10.02	1.29	13.66	8.29
2	14.95	5.65	27.71	8.96	12.73	3.90	24.76	8.10
3	16.69	3.45	24.30	11.27	21.71	4.91	29.60	12.97
4	20.54	4.41	29.28	14.85	22.57	3.58	32.19	16.74
5	28.71	10.65	60.50	14.17	32.89	3.69	40.73	25.76

rms delay spread were performed in a smaller window to avoid misleading results.)

From Table IV it can be seen that for vertically polarized reception, the predicted rms delay spread agrees remarkably well with the measured value. Only Point 5 (NLOS) shows some deviation, with the simulation overpredicting by approximately 9 ns. As shown in Table V, for the horizontally polarized receiver as well the predictions are very close to the measured values of rms delay spread. Moreover, not only the mean value, but also the other statistics are very well predicted by the model. Hence, it can be concluded that although high accuracy in the simulated impulse responses can be difficult to achieve, the model can provide very good predictions for the wide-band statistics of the radio channel.

B. Comparison Between Measured and Predicted RMS Delay Spread along an NLOS Route

Continuing the investigation into the wide-band predictions of the indoor propagation model, in this section the rms delay spread values of measured profiles along the route shown in Fig. 16 are compared with simulation results. Unlike the measurement strategy of the previous section, the results were not inverse Fourier transformed to the time domain internally in the network analyzer. Instead, the channel frequency responses were obtained (401 samples over a bandwidth of 200 MHz) and the channel impulse responses were acquired after performing inverse Fourier transform on the measured results (using a Kaiser window with beta $=3.5$ [25]).

In a manner similar to the process used for the comparison between measured and predicted channel impulse responses in the previous section, for each point eight profiles were measured within an area of approximately 1 m^2. The time dispersion of each profile was calculated and the average rms delay spread of the eight profiles at each point was then obtained. Fig. 29 depicts the mean measured rms delay spread along the route, together with the minimum and maximum values at each point for a vertically orientated receiver. As shown in the figure, the rms delay spread varies by as much as 18 ns at some points. The standard deviation of the measured values along the route is on average 3.38 ns for the vertical receiving dipole and 3.24 ns for the horizontal one.

The predicted infinite bandwidth impulse responses were again transformed to the limited bandwidth of the measurements. This time the transformation was performed by

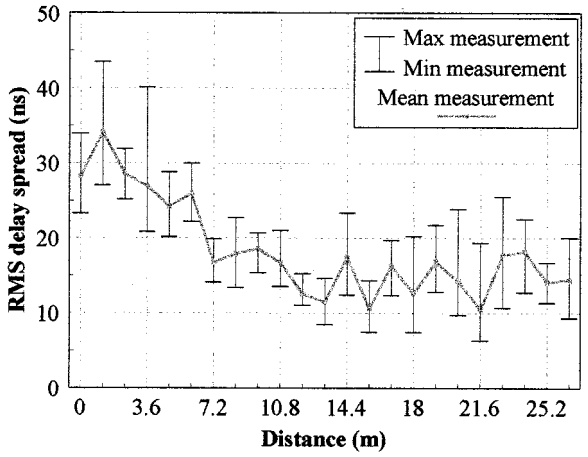

Fig. 29. Measured rms delay spread along the corridor for a vertically polarized receiver.

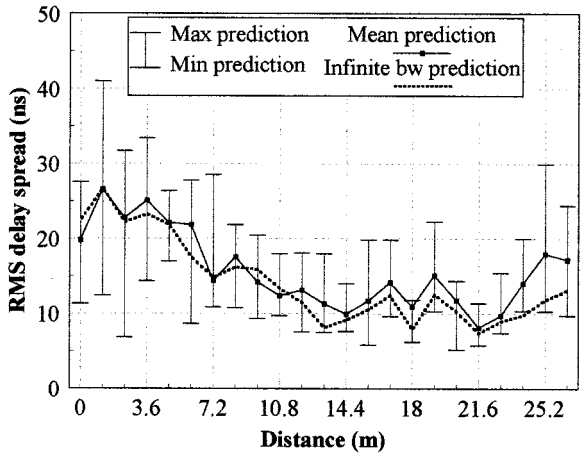

Fig. 30. The rms delay spread predictions for a vertically polarized receiving dipole.

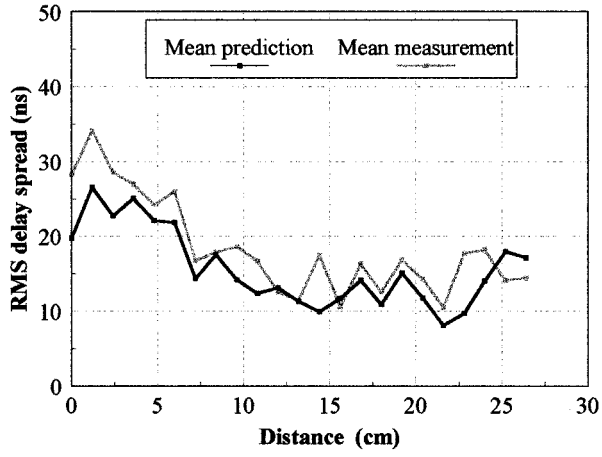

Fig. 31. Mean measured and predicted rms delay spread for a vertical receiving dipole.

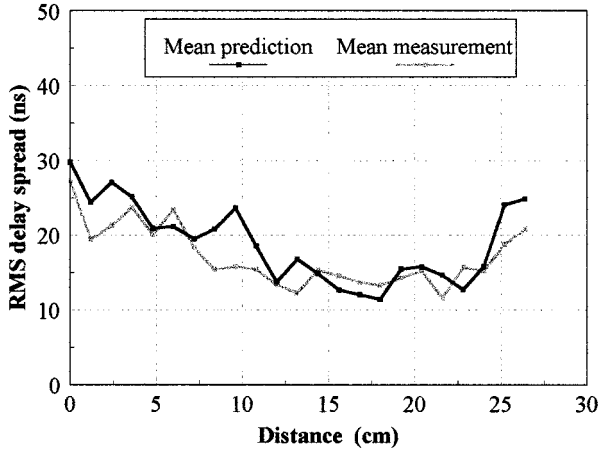

Fig. 32. Mean measured and predicted rms delay spread for a horizontal receiving dipole.

convolving the ray-tracing response with the inverse Fourier transform of a Kaiser window with 200-MHz bandwidth. Similarly to the measurements, a grid analysis of nine points (3×3) was performed over a 1.2×1.2-m area at each point, in order to calculate the average predicted rms delay spread (shown in Fig. 30 for the vertical receiving dipole, together with the minimum and maximum predicted values). As with the measured value, the predicted rms delay spread can vary severely at each point. The standard deviation of the simulated values along the route is on average 4.07 ns for the vertical dipole and 4.42 ns for the horizontal one. In this case, the increased fluctuation of the predictions compared to the measured values is due to the more abrupt changes of the simulated environment because of the infinitely thin walls. The average rms delay spread values for the predicted channel impulse responses with infinite bandwidth are also shown in Fig. 30 and follow the trend of the finite bandwidth results for the majority of the route.

The mean measured and predicted values of rms delay spread along the route for a vertically orientated receiver are depicted in Fig. 31. The simulation results follow closely the trend and the values of the measurements with a mean error of -2.77 ns and a standard deviation of 3.3 ns (Table VI). After normalization to the measurements, the mean error is 0.1 and the standard deviation is 0.18. In the cross-polar case as well, the predictions are close to the measured values, as shown in Fig. 32. The mean error along the route is 1.81 ns and the standard deviation is 2.97 ns, while the normalized mean error and standard deviation are 0.13 and 0.18, respectively. From the above results, it can be concluded that with sufficient representation of the indoor environment, the ray-tracing model is capable of accurately predicting the wide-band characteristics of a radio channel even in NLOS areas.

VI. Conclusion

In this paper, a novel 3-D ray-tracing propagation algorithm was presented. The model applies GO and UTD in order to calculate the electromagnetic field of each ray, using complex vector analysis and 3-D radiation patterns. In order to determine the geometry of the rays, a hybrid imaging technique has been developed according to which 2-D image generations in vertical and horizontal planes are combined to produce 3-D paths. The algorithm is able to support the modeling of the ceiling, floor and other horizontal surfaces, such as tables and benches, as

TABLE VI
ERROR STATISTICS FROM THE COMPARISON BETWEEN MEASURED AND PREDICTED RMS DELAY SPREAD VALUES

	Mean error (ns)	Standard deviation (ns)	RMS error (ns)
Co-polar antennas	-2.7739	3.3098	4.3185
Cross-polar antennas	1.8095	2.9703	3.4781

well as walls with multiple windows and doors, and also partitions. Moreover, rays whose paths fall partially outside of the buildings are modeled, and, hence, external building structures can be considered. Another significant characteristic of the presented algorithm is that each image is associated with a specific area for which the image can give a valid path, the *illumination zone*. This technique greatly simplifies the image map and allows the evaluation of complex indoor scenarios. Because of the smaller number of images, but also because the images which illuminate a mobile position can now be identified very easily, the path tracing is significantly accelerated.

In order to investigate the accuracy of the presented model, comparisons of predictions with measurements were performed in LOS, NLOS, and deep shadow areas, both for co- and cross-polarized antennas. The analysis shows that accurate power predictions can be achieved with rms errors less than 7 dB, even when large sections of the test route are in deep shadow areas. In the NLOS regions close to the transmitter, the rms error is below 3 dB for both receiving antenna polarizations. Predictions emulating the measurement process showed that deviations between measured and simulated results can exist due to the limited averaging of the measurements. The comparison with measurements also revealed that because of the simulation of the walls as infinitely thin, under NLOS conditions the predictions follow the measurements with a spatial delay and even predict areas of high power where in fact the powerful rays are blocked. Hence, attention must be paid in the modeling of indoor environments when transmission through walls is active.

A comparison between measured and predicted channel impulse responses provided an insight into both the real and modeled radio channels. It was seen that in the case of copolarized antennas the power profile is determined by a few dominant rays, and if the prediction for one of these rays is inaccurate, then the deviation between measured and simulated profiles is considerable. In the cross-polar case, the dominant rays are weaker and the scatterers become more important, but the results are more stable, since they are determined by more rays. The heavily delayed rays are more difficult to predict because the longer it takes a ray to reach the receiver, the more likely it is for this ray to be blocked in reality. Also, the more a ray interacts with the environment, the more the cumulative error caused by the estimations of the wall coefficients increases.

Generally, the ray-tracing model managed to identify the major paths of the channel impulse responses and their time delays and thus followed the trend of the measured power profiles in most cases and for both co- and cross-polarized antennas. Although it was not possible to predict the exact profile shapes, the predicted rms delay spread values agreed well with those measured. Along an NLOS route, the rms delay spread was predicted with an rms error less than 5 ns and a normalized mean error less than 13% for both receiving antenna orientations. Hence, although high accuracy in the simulated impulse responses can be difficult to achieve, the model can provide very good predictions for the wide-band statistics of the radio channel even in NLOS areas.

ACKNOWLEDGMENT

The authors thank Prof. J. P. McGeehan for the provision of laboratory facilities and Dr. G. V. Tsoulos for his constructive suggestions and help with the measurement campaign.

REFERENCES

[1] W. Honcharenko, H. L. Bertoni, J. L. Dailing, J. Qian, and H. D. Yee, "Mechanisms governing UHF propagation on single floors in modern office buildings," *IEEE Trans. Veh. Technol.*, vol. 41, pp. 496–504, Nov. 1992.

[2] R. A. Valenzuela, "A ray tracing approach to predicting indoor wireless transmission," in *IEEE VTC'93*, May 18–20, 1993, pp. 214–218.

[3] M. C. Lawton and J. P. McGeehan, "The application of a deterministic ray launching algorithm for the prediction of radio channel characteristics in small-cell environments," *IEEE Trans. Veh. Technol.*, vol. 43, pp. 955–969, Nov. 1994.

[4] U. Dersch and E. Zollinger, "Propagation mechanisms in microcell and indoor environments," *IEEE Trans. Veh. Technol.*, vol. 43, pp. 1058–1066, Nov. 1994.

[5] S. Y. Seidel and T. S. Rappaport, "Site-specific propagation prediction for wireless in-building personal communications system design," *IEEE Trans. Veh. Technol.*, vol. 43, pp. 1058–1066, Nov. 1994.

[6] G. E. Athanasiadou, A. R. Nix, and J. P. McGeehan, "A new 3-D indoor ray tracing model with particular reference to predictions of power and rms delay spread," in *IEEE PIMRC '95*, Toronto, Canada, Sept. 1995, pp. 1161–1165.

[7] S. Y. Tan and H. S. Tan, "UTD propagation model in an urban street scene for microcellular communications," *IEEE Trans. Electromag. Compat.*, vol. 35, pp. 423–428, Nov. 1993.

[8] K. R. Schaubach and N. J. Davis IV, "Microcellular radio-channel propagation prediction," *IEEE Antennas Propagat. Mag.*, pp. 25–34, Aug. 1994.

[9] K. Rizk, J.-F. Wagen, and F. Gardiol, "Two-dimensional ray-tracing modeling for propagation prediction in microcellular environments," *IEEE Trans. Veh. Technol.*, vol. 46, pp. 508–518, May 1997.

[10] V. Erceg, S. J. Fortune, J. Ling, A. J. Rustako, and R. A. Valenzuela, "Comparisons of a computer-based propagation prediction tool with experimental data collected in urban microcellular environments," *IEEE J. Select. Areas Commun.*, vol. 15, pp. 677–684, May 1997.

[11] G. E. Athanasiadou, A. R. Nix, and J. P. McGeehan, "A microcellular ray-tracing propagation model and evaluation of its narrowband and wideband predictions," *IEEE J. Select. Areas Commun.*, vol. 18, Mar. 2000.
[12] C. A. Balanis, *Advanced Engineering Electromagnetics*. New York: Wiley, 1989.
[13] J. B. Keller, "Geometrical theory of diffraction," *J. Opt. Soc. Amer.*, vol. 52, pp. 116–130, Feb. 1962.
[14] R. G. Kouyoumjian and P. H. Pathak, "A uniform geometric theory of diffraction for an edge on a perfectly conducting surface," *Proc. IEEE*, vol. 62, pp. 1448–1461, Nov. 1974.
[15] R. J. Luebbers, "Finite conductivity uniform GTD versus knife edge diffraction in prediction of propagation path loss," *IEEE Trans. Antennas Propagat.*, vol. AP-32, pp. 70–76, Jan. 1984.
[16] G. L. Turin *et al.*, "A statistical model for urban multipath propagation," *IEEE Trans. Veh. Technol.*, vol. VT-21, pp. 1–9, Feb. 1972.
[17] S. J. Fortune, D. M. Gay, B. W. Kernigham, O. Landron, R. A. Valenzuela, and M. H. Wright, "WISE design of indoor wireless systems: Practical computation and optimization," *IEEE Comput. Sci. Eng.*, pp. 58–68, 1995.
[18] A. R. Nix, G. E. Athanasiadou, and J. P. McGeehan, "Predicted HIPERLAN coverage and outage performance at 5.2 GHz and 17 GHz using indoor 3-D ray-tracing techniques," *Wireless Personal Commun. J.*, vol. 3, no. 4, pp. 365–388, 1996.
[19] G. E. Athanasiadou, "Propagation assessment of home environment report," ESPRIT WINHOME Project Rep. WP2.2a-1, Aug. 1998.
[20] M. R. Williamson, G. E. Athanasiadou, and A. R. Nix, "Analysis of antennas and propagation for 60 GHz indoor wireless networks," in *Insights into Mobile Multimedia Communications*, D. Bull, N. Canagarajah, and A. Nix, Eds. New York: Academic, 1999, ch. 39, pp. 609–635.
[21] P. Beckmann and A. Spizzichino, *The Scattering of Electromagnetic Waves from Rough Surfaces*. New York: Pergamon, 1963.
[22] A. R. Von Hippel, *Dielectric Materials and Applications*. New York: Wiley, 1954.
[23] *American Institute of Physics Handbook*, 3rd ed. New York: McGraw-Hill, 1972.
[24] R. A. Valenzuela, O. Landron, and D. L. Jacobs, "Estimating local mean signal strength of indoor multipath propagation," *IEEE Trans. Veh. Technol.*, vol. 46, pp. 203–210, Feb. 1997.
[25] F. J. Harris, "On the use of windows for harmonic analysis with discrete Fourier transform," *Proc. IEEE*, vol. 66, pp. 51–84, Jan. 1978.

Georgia E. Athanasiadou (M'00) received the M.S. degree in electrical and computer engineering from the National Technical University of Athens, Greece, in 1992 and the Ph.D. degree from the University of Bristol, Bristol, U.K., in 1997.

From October 1996 until October 1999, she was a Research Associate and then a Research Fellow at the Centre for Communications Research, University of Bristol, working in the area of radio propagation modeling. As part of her research she has developed, investigated, and evaluated novel indoor and outdoor ray tracing propagation models. Her research interests include network planning issues with ray tracing models for different air interface techniques, with particular emphasis on adaptive antennas and future generation systems. She is now a Senior Research Engineer with Adaptive Broadband Ltd., Cambridge, U.K. working on broadband systems.

Dr. Athanasiadou is a member of the Technical Chamber of Greece.

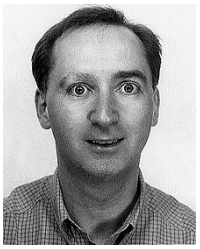

Andrew R. Nix (A'97) was awarded B.Eng. and Ph.D. degrees in electrical and electronic engineering from the University of Bristol, in 1989 and 1993, respectively. Following his Ph.D. he was appointed to a lecturing position at the University of Bristol. In 1999 he was promoted to his current position as Reader in the area of Digital Communications.

His main research interests include wireless propagation, modulation and wireless LANs. He currently heads the propagation modelling and wireless LAN groups in the Centre for Communications Research.

In the area of Wireless LANs, he has managed Bristol's contribution in a number of collaborative European projects. In the area of propagation modelling, his research group has produced leading propagation models based on site specific ray tracing and radar cross section techniques. He has published in excess of 130 journal and conference papers and is a member of ETSI BRAN.